ELSEVIER

Soil Dynamics and Earthquake Engineering 26 (2006) 377–394

SOIL DYNAMICS AND EARTHQUAKE ENGINEERING

www.elsevier.com/locate/soildyn

Static and dynamic response of massive caisson foundations with soil and interface nonlinearities—validation and results

Nikos Gerolymos, George Gazetas *

National Technical University, Athens, Greece

Accepted 3 December 2005

Abstract

The static, cyclic, and dynamic response of a massive caisson foundation embedded in nonlinear layered or inhomogeneous soil and loaded at its top is investigated. The caisson is supported against horizontal displacement and rotation by four types of inelastic springs and dashpots, described with the BWGG model that was developed in the preceding companion paper [Gerolymos N, Gazetas G. Development of winkler model for static and dynamic response of caisson foundations with soil and interface nonlinearities. Soil Dyn Earthq Eng, submitted companion paper]. The prediction of the model is satisfactorily compared with results from 3D-finite element analysis. *Some* experimental corroboration of the method is provided with the help of a 1/3-scale lateral load test that had been conducted in the field by EPRI. An illustrative example of a caisson embedded in linearly-inhomogeneous clay and subjected to static and dynamic loading is analysed. Characteristic results are presented highlighting the role of soil inelasticity and its interplay with the two dominant interface nonlinearities: separation (gapping) of the caisson shaft from the surrounding soil, and uplifting of the base from the underlying soil.

Keywords: Winkler model; Soil–foundation interaction; Cyclic loading; 3D-finite element analysis load test validation; Nonlinear response; Sliding; Uplifting

1. Introduction

This paper is the third in a sequence of four papers dealing with the static, cyclic and seismic response of massive caissons, of circular, square, or rectangular plan shape, embedded in linear and nonlinear soil.

The first paper [2] studied the inertial and kinematic seismic response of a caisson embedded in an elastic homogeneous halfspace. A key feature of that paper was the development of a generalized Winkler model, involving four types of springs—distributed translational and rotational springs along the height of the caisson shaft, and concentrated swaying and rocking springs at the caisson base. Analytical (although not always closed-form) expressions for the moduli of those springs (and of the associated dashpots) were obtained by calibrating the model against published elastodynamic solutions.

The second paper [1] recognized the profound role of soil and interface nonlinearities in the response of a caisson subjected to strong static or dynamic excitation. It thus developed a most general inelastic Winkler model, in which each type of 'spring' was described through a nonlinear differential equation of the Bouc-Wen (BW) type, as is known in the literature; our version of this model, dubbed BWGG model, was shown to possess the versatility to describe with sufficient realism such phenomena as separation and slippage at the caisson shaft–soil interface, uplift of the caisson base from the underlying soil, radiation damping, and stiffness and strength degradation with increasing number of cycles.

In this third paper, we study the dynamic response to externally applied loading of a massive caisson, supported by the inelastic springs described by the BWGG model of the second paper. The emphasis now is:

- on the validation of the nonlinear method through comparisons with (a) 3D-finite element analysis, and (b) 1/3-scale lateral load test
- on the presentation of characteristic results that shed light on the role of the aforementioned nonlinearities in the behaviour of the caisson, statically and dynamically.

2. Caisson response to static, cyclic, and dynamic lateral loading

The problem is that of a square or circular caisson embedded in a layered soil, and subjected to lateral motion as shown in Fig. 1. The caisson is considered to be rigid with mass m, and mass moment of inertia about the center of gravity

* Corresponding author.
E-mail address: gazetas@ath.forthnet.gr (G. Gazetas).

0267-7261/$ - see front matter © 2005 Elsevier Ltd. All rights reserved.
doi:10.1016/j.soildyn.2005.12.001

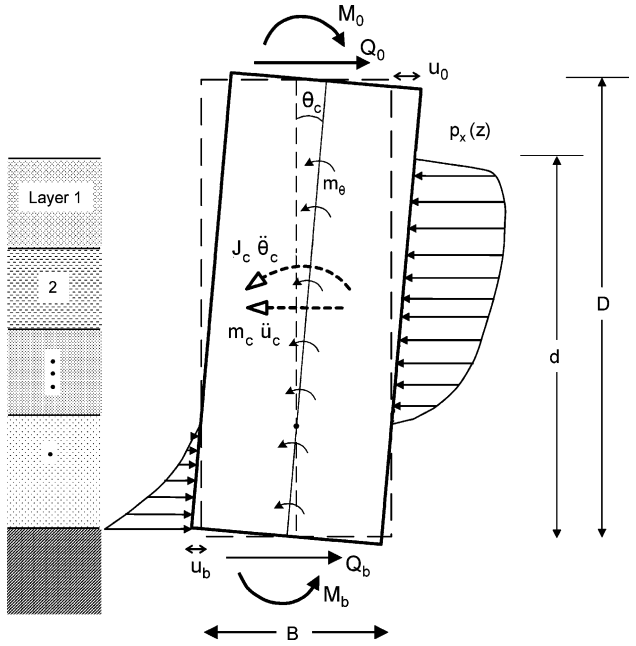

Fig. 1. Displacement of, and forces on, a caisson subjected to lateral dynamic loading (Q_0, M_0) at its top.

J_c. The depth of embedment is D, while the height of the sidewall in contact with the surrounding soil is d. The nonlinear Winkler model described in the previous sections is used for simulating the soil–caisson interaction.

Dynamic horizontal force equilibrium gives

$$Q_0 - m\ddot{u}_c - P_x - Q_b = 0 \tag{1}$$

and dynamic rotational equilibrium with respect to the base of the caisson

$$M_0 + Q_0 D - J_c\ddot{\theta} - m\frac{D}{2}\ddot{u}_b - M_x - M_\theta - M_b = 0 \tag{2}$$

where $Q_0 = Q_0(t)$ and $M_0 = M_0(t)$ are the time-dependent external horizontal force and overturning moment applied at the top of the caisson, u_c and $\ddot{u}_c$ are the displacement and acceleration at the center of the caisson; θ and $\ddot{\theta}$ are the rotation and rotational acceleration of the caisson block; and u is the horizontal displacement at a particular depth of the caisson, related to u_c and θ

$$u = u_c\left(z - \frac{D}{2}\right)\theta \tag{3}$$

$P_x = P_x(t)$ is the total sidewall horizontal resistance, i.e. the resultant of the distributed lateral soil reactions

$$P_x = \int_0^d [p_s(z) + p_d(z)]\mathrm{d}z \tag{4}$$

where:

- the 'restoring' force (per unit depth) $p_s = p_s(z)$ is inelastically related to the horizontal displacement u at each particular depth

$$p_s = \alpha_x k_x u + (1-\alpha_s)p_y\zeta_x \tag{5}$$

in which ζ_x is a dimensionless factor, obeying the following differential equation with respect to time t

$$\frac{\mathrm{d}\zeta_x}{\mathrm{d}t} = \lambda_x\frac{h_x}{u_y}\left[\frac{\mathrm{d}u}{\mathrm{d}t} - (1+r_x)\left(b_x\frac{\mathrm{d}u}{\mathrm{d}t}|\zeta_x|^{n_x} + g_x\left|\frac{\mathrm{d}u}{\mathrm{d}t}\right||\zeta_x|^{n_x-1}\zeta_x\right)\right] \tag{6}$$

The meaning of the various parameters in the above equations can be found in the companion paper by the authors [1] and will not be repeated here.

- The '*dissipative*' force $p_d = p_d(z)$ relates also inelastically to the horizontal velocity, $\dot{u}$, at each particular depth

$$p_d = c_x\dot{u}\left[a_x + (1-a_x)\frac{\partial\zeta_x}{\partial u}\right]^{c_{sd}} \tag{7}$$

with the symbols explained in the aforesaid companion paper.

$Q_b = Q_b(t)$ is the resultant shear (horizontal) force at the base of the caisson, expressed in the differential form similar to p_s and p_d for its 'restoring' and 'dissipative' components, respectively. Refer to the companion paper [1].

$M_x = M_x(t)$ and $M_\theta = M_\theta(t)$ are the resultant moments of the distributed sidewall tractions; the first, due to the lateral soil reactions (producing moments with respect to the base), and the second due to the vertical shear tractions on the caisson periphery (producing moments m_θ at each depth)

$$M_x = \int_0^d [p_s(z) + p_d(z)]z\,\mathrm{d}z \tag{8}$$

$$M_\theta = \int_0^d [m_s(z) + m_d(z)]\,\mathrm{d}z \tag{9}$$

In this last expression, the 'restoring' moment (per unit depth) $m_s = m_s(z)$ is inelastically related to the rotation θ at each particular depth through a dimensionless parameter ζ_θ. The latter satisfies a differential equation analogous in form to Eq. (6). The 'dissipative' moment (per unit depth) $m_d = m_d(z)$ relates also inelastically to the horizontal angular velocity,$\dot{\theta}$, at each particular depth, in a form analogous to Eq. (7).

Finally, $M_b = M_b(t)$ is the resultant moment reaction at the base of the caisson, the 'restoring' and 'dissipative' components of which are expressed in differential form similar to that of Eqs. (5)–(7).

The details of the foundation and the meaning of all the parameters involved can be found in the companion paper [1].

We thus have a system of 6 coupled differential equations: two second-order (Eqs. (1) and (2)) and four first-order (such as Eq. (6), and the analogous equations mentioned above). An explicit finite-difference algorithm has been developed for the solution of this system. The algorithm was incorporated

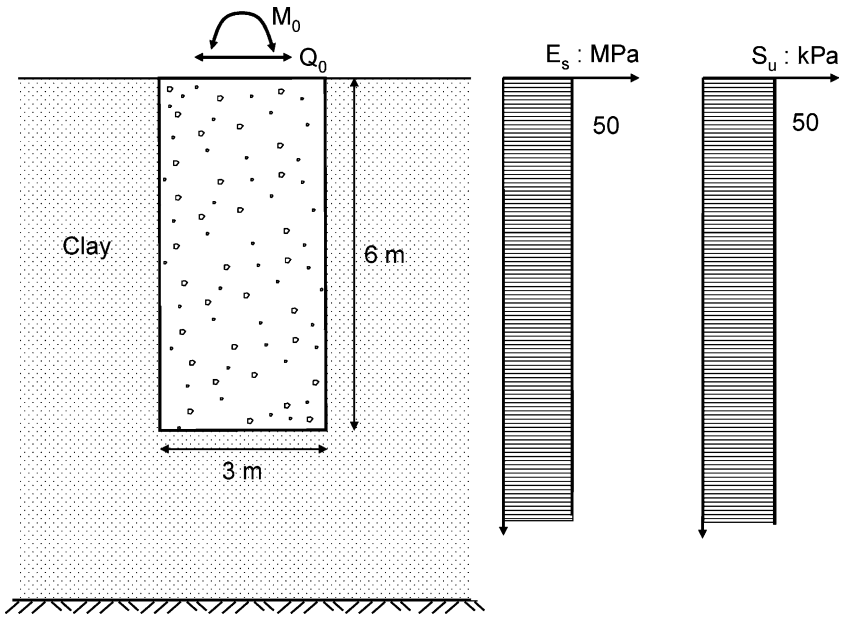

Fig. 2. First example problem for the lateral response of a caisson to monotonic (Case A) and dynamic (Case B) loading at its top.

into a (new) computer code, NL-CAISSON, for the nonlinear analysis of caissons under lateral loading [1].

3. Comparison with results of 3D finite-element analysis

The capability of the model is investigated through comparison with results of finite element analyses. The problem studied is portrayed in Fig. 2: a rigid circular caisson of height $D=6$ m and diameter $B=3$ m, embedded in cohesive soil stratum, and laterally loaded at its head. Young's modulus, Poisson's ratio, mass density, and undrained shear strength of the soil are constant with depth: $E_s=50$ MPa, $\nu_s=0.3$, $\rho_s=2$ Mg/m^3, and $S_u=50$ kPa. A detailed numerical model of the caisson and the surrounding soil is developed with the finite element code ABAQUS. Both caisson and soil are modelled with three-dimensional elements. The far field is represented with infinite elements, ensuring that the displacements vanish 'at infinity' (correct reproduction of radiation damping). The soils stratum reaches 10 m deeper than the caisson base, thus having a negligible influence on the response. The caisson is rigidly connected to the surrounding soil. In other words slippage in caisson–soil interface and separation of the caisson from the soil are not allowed. To ensure uniform stress distribution at the head of the caisson, the nodes of the associated elements are properly kinematically constrained. Inelastic soil behaviour is described through the Von-Mises yield surface with nonlinear kinematic hardening and an associative plastic flow rule.

Two cases are considered: static and dynamic loading, at the head of the caisson, each of subdivided into two cases with different loading paths, as follows:

- Case A: static loading
  A1: shear force of 5 MN applied monotonically.
  A2: combined shear force and overturning moment of

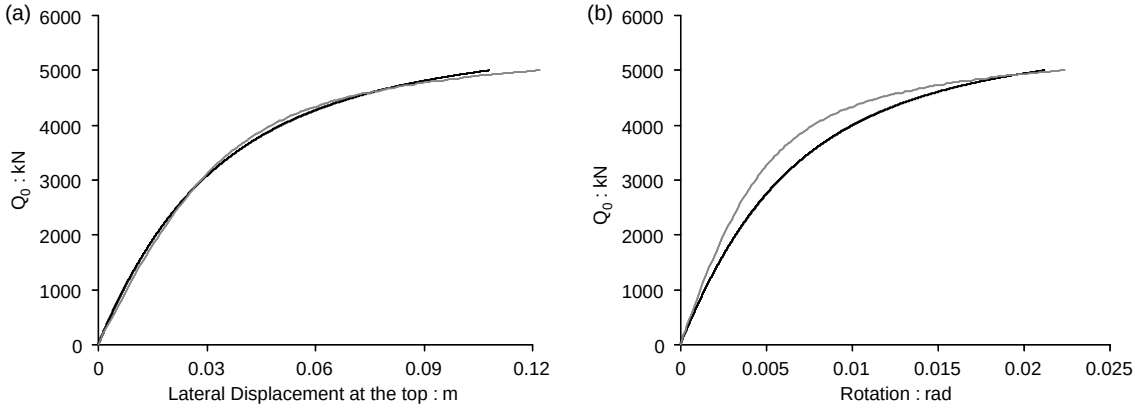

Fig. 3. Comparison of computed with the finite element model (grey line), and predicted with the proposed model for caissons (black line) of: (a) horizontal force–displacement and (b) horizontal force–rotation curves at the top of the caisson ('pushover' curves), for Case A1 (a 5000 kN shear force monotonically applied at the head of the caisson).

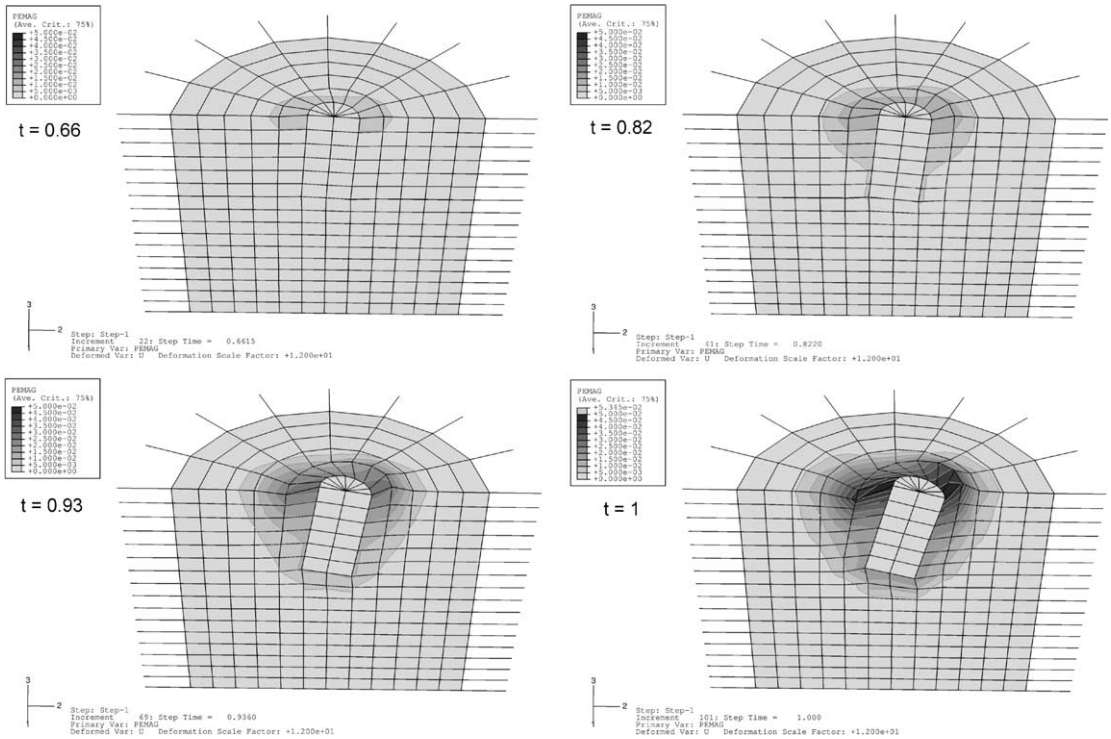

Fig. 4. Contours of plastic strain magnitude (plotted on the deformed mesh) at selected loading levels (as a fraction of the total applied load) for case A1 (a 5000 kN shear force monotonically applied at the head of the caisson).

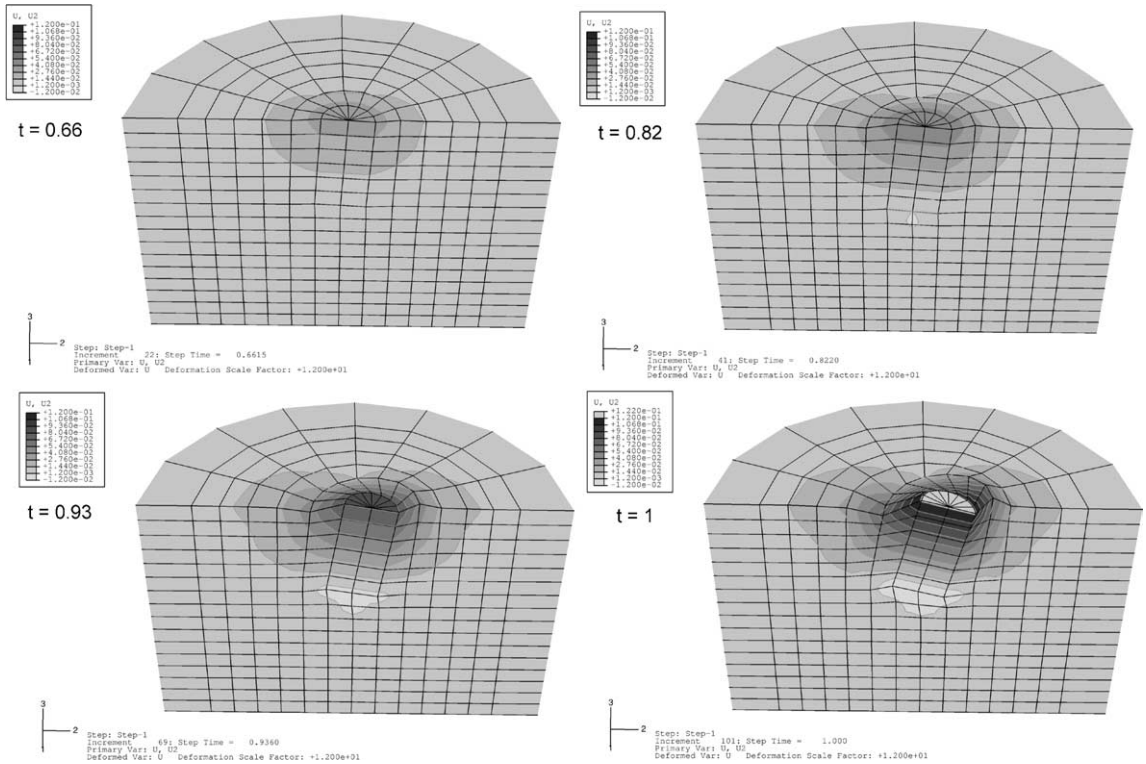

Fig. 5. Contours of horizontal displacement (plotted on the deformed mesh) at selected loading levels (as a fraction of the total applied load) for Case A1 (a 5000 kN shear force monotonically applied at the head of the caisson).

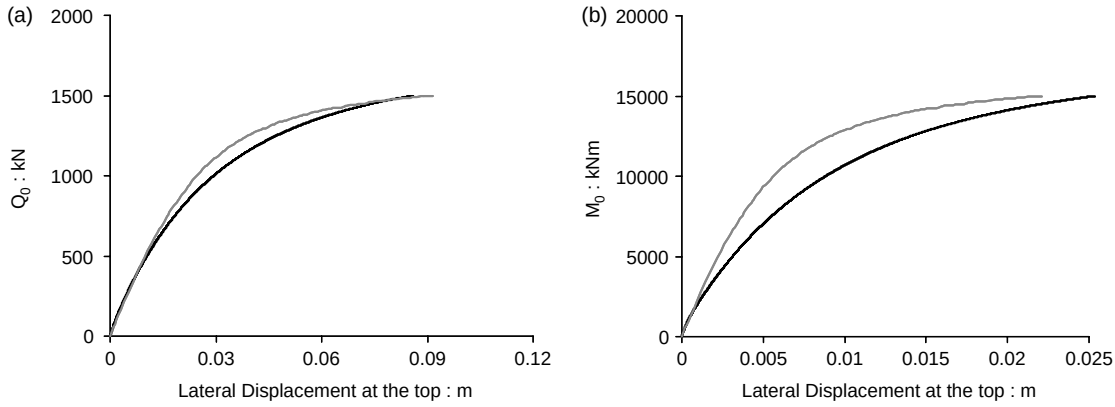

Fig. 6. Comparison of computed with the finite element model (grey line), and predicted with the proposed model for caissons (black line) of: (a) horizontal force–displacement and (b) moment–rotation curves at the top of the caisson ('pushover' curves), for Case A2 (a combined 1500 kN shear force and 15,000 kNm overturning moment monotonically applied at the head of the caisson).

1.5 MN and 15 MNm, respectively, applied monotonically.

- Case B: dynamic loading
  - B1: four cycles of a 2 Hz sinusoidal horizontal force of 5 MN amplitude.
  - B2: four cycles of a 2 Hz sinusoidal horizontal force of 1.5 MN amplitude and overturning moment of 15 MNm amplitude.

The calibration of the parameters of the two models is based on a methodology, presented below, according to which the BWGG model and the plasticity model of ABAQUS yield the same results in a unidirectional stress–strain test.

The calibration of the model parameters of the two models is based on a methodology, presented below, according to which the BWGG model and the plasticity model of ABAQUS yield the same results in a unidirectional stress–strain loading test. In ABAQUS, integration of the 'back-stress' evolution law over a half cycle of unidirectional load (e.g. tension or compression) yields the following expression

$$a = \frac{C}{\gamma}[1 - \exp(-\gamma\varepsilon^{\mathrm{pl}})] \tag{10}$$

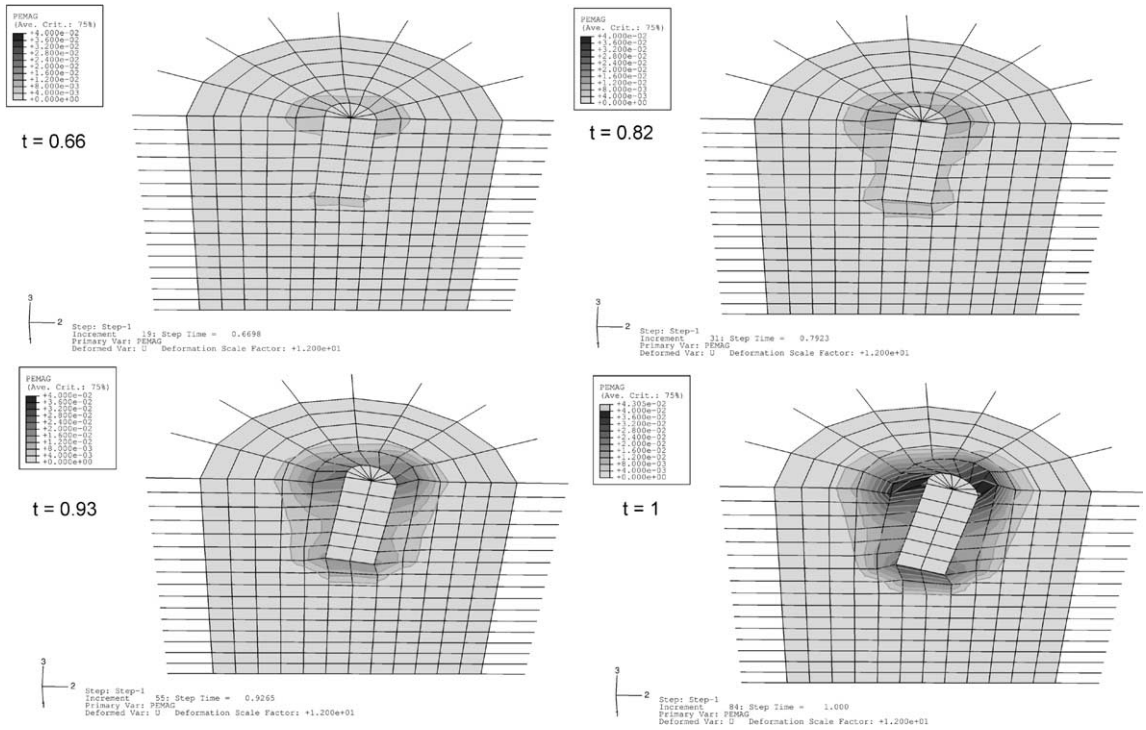

Fig. 7. Contours of plastic strain magnitude (plotted on the deformed mesh) at selected loading levels (as a fraction of the total applied load) for Case A2 (a combined 1500 kN shear force and 15,000 kNm overturning moment monotonically applied at the head of the caisson).

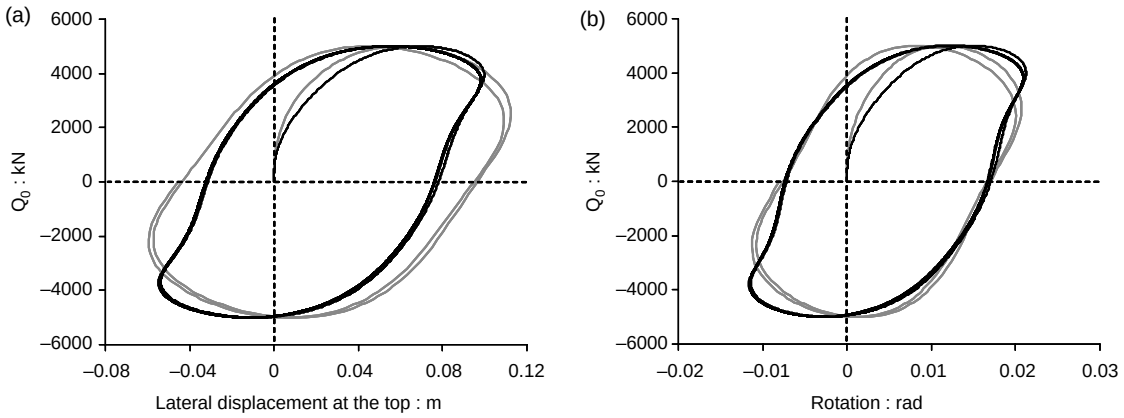

Fig. 8. Comparison of computed with the finite element model (grey line), and predicted withy the proposed model for caissons (black line) of: (a) horizontal force versus displacement and (b) horizontal force versus rotation loops at the top of the caisson, for Case B1 (four cycles of 2 Hz sinusoidal 5000 kN horizontal force, applied at the head of the caisson).

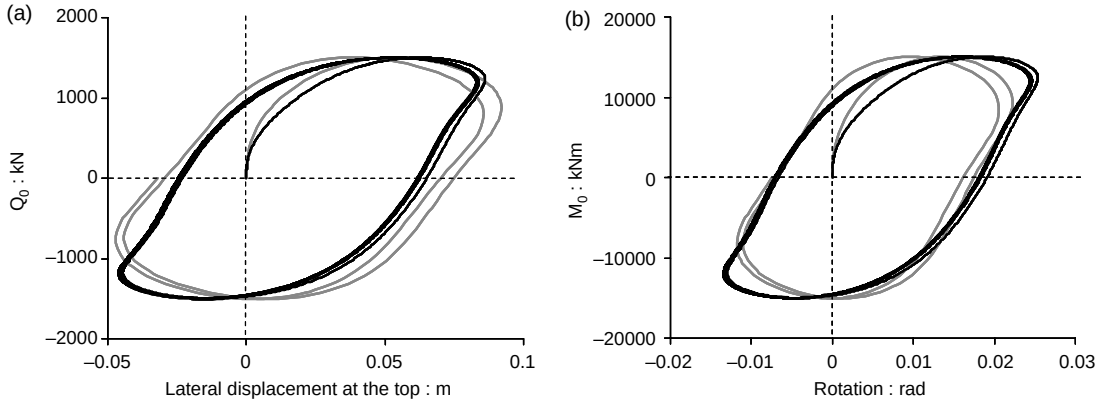

Fig. 9. Comparison of computed with the finite element model (grey line), and predicted with the proposed model for caissons (black line) of: (a) horizontal force versus displacement and (b) moment versus rotation loops at the top of the caisson, for Case B2 (four cycles of combined 2 Hz sinusoidal 1500 kN horizontal force and 15,000 kNm overturning moment, applied at the head of the caisson).

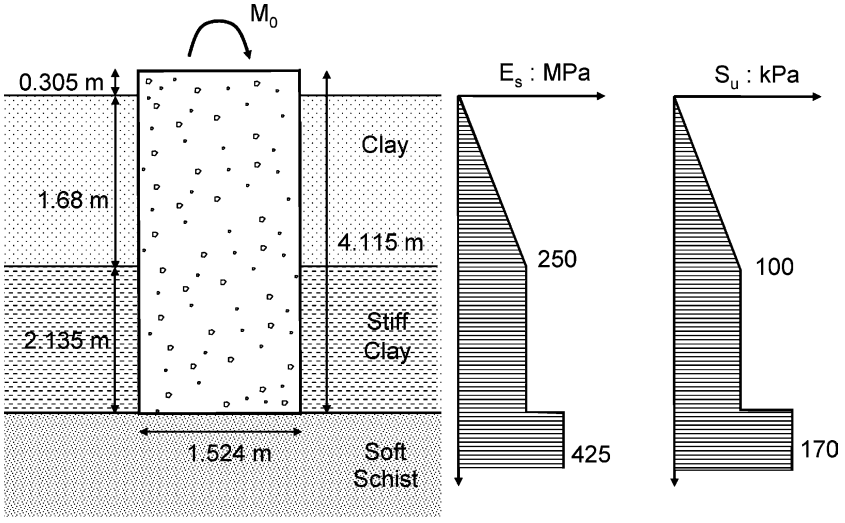

Fig. 10. Idealized soil profile and caisson geometry of the in situ caisson load test carried out by EPRI (1981). M_0 was increased up to failure of the caisson–soil system.

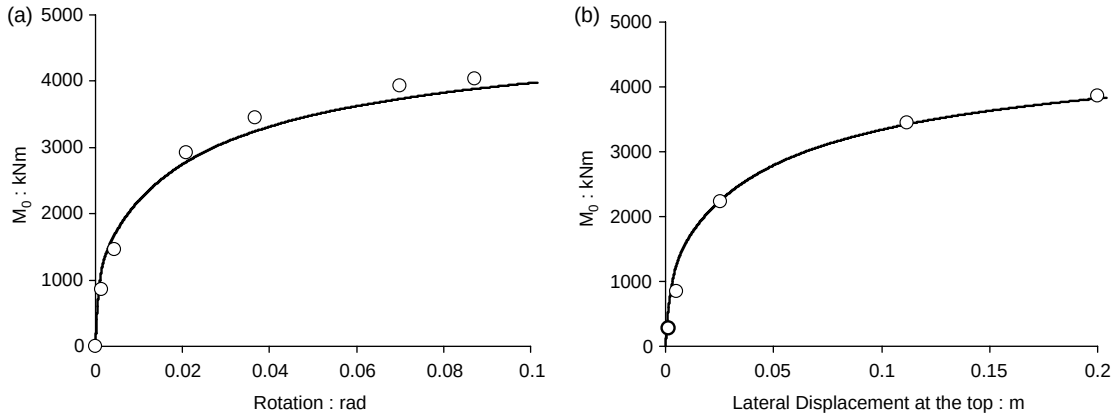

Fig. 11. EPRI caisson static load test [3]: comparison of the computed (solid line) (a) moment–rotation and (b) moment–displacement curves at the top of the caisson with (b) the experimental data points (circles).

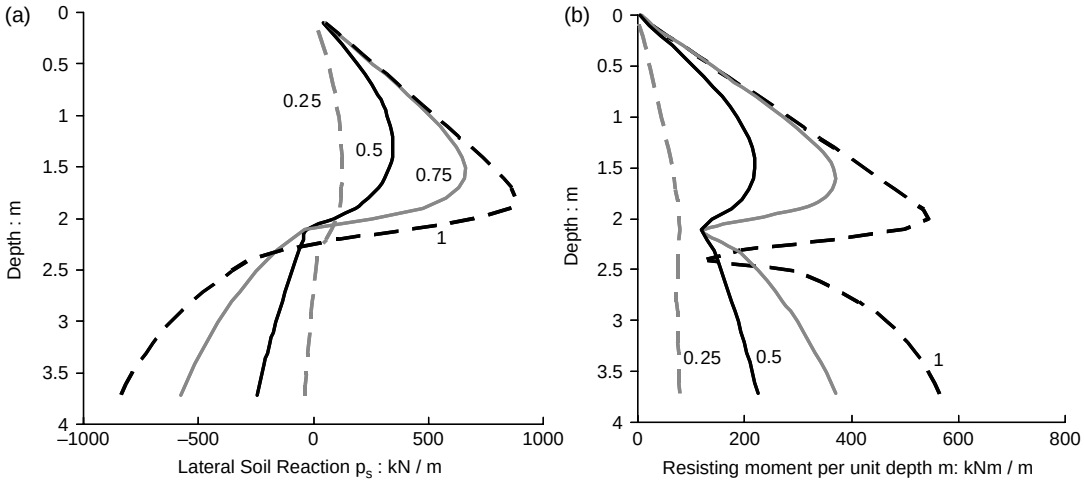

Fig. 12. Computed profiles of distributed (a) soil horizontal reaction and (b) moment reaction at selected loading levels M_0/M_u for the caisson of Fig. 2.

in which α is the back-stress that defines the kinematic evolution of the yield surface, C and γ are hardening parameters that define the maximum transition of the yield surface, and the rate of transition, respectively. ε^{pl} is the plastic strain. The current value of stress σ is then expressed according to

$$\sigma = \sigma_0 + a \tag{11}$$

in which σ_0 the value of σ at zero plastic strain. The unidirectional stress–strain relationship of a soil element according to the BWGG constitutive model is given by

$$\sigma = \sigma_y \zeta \tag{12}$$

in which σ_y is the maximum yield stress and ζ is the hysteretic parameter that controls the nonlinear stress–strain behaviour, defined in the second companion paper [1]. In monotonic loading conditions and accepting Masing rule for unloading–reloading and $n=1$. ζ is expressed in the following analytical form

$$\zeta = 1 - \exp(-\varepsilon/\varepsilon_y) \tag{13}$$

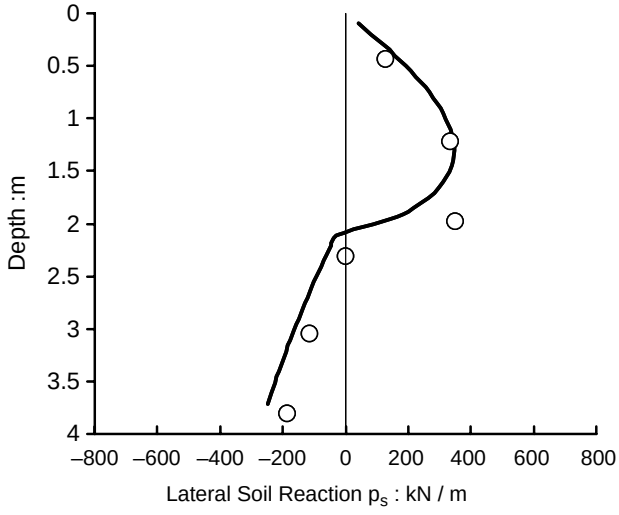

Fig. 13. EPRI caisson static load test (1981): comparison of the computed (black solid line) and recorded (circles) soil reaction profiles, at loading level $M_0/M_u=0.5$.

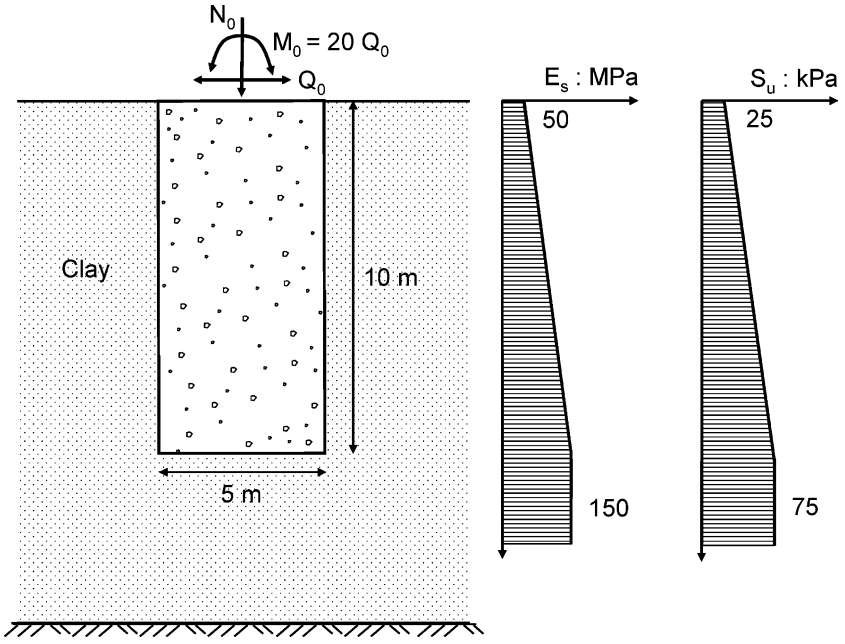

Fig. 14. Second example problem for the lateral response of a caisson to monotonic (Case a) and dynamic (Case b) loading at its top. The second case is subdivided into: (b1) where only material (soil) nonlinearity is considered, and (b2) where both interface and soil nonlinearities are considered. In all the cases, a constant vertical load is applied atop the caisson.

in which ε is the strain, and ε_y a characteristic strain which is a measure of yielding. Notice that Eqs. (10), (12) and (13) are of similar form. Equating them leads to

$$\gamma = \frac{1}{\varepsilon_y}, \qquad C = \frac{\sigma_y}{\varepsilon_y}, \quad \text{and} \quad \sigma_0 = 0 \tag{14}$$

while, by definition, $C=\sigma_y/\varepsilon_y=E$

In the Von-Mises yielding criterion, the maximum yield stress is equal to

$$\sigma_y = \sqrt{3}S_u \tag{15}$$

Thus, the hardening parameter is

$$\gamma = \frac{E}{\sqrt{3}S_u} \tag{16}$$

Thus, the hardening parameters of the plasticity model are: $C=50{,}000$, $\gamma=577$. For the BWGG model: $n_x=n_r=n_h=n_\theta=1$; $\alpha_x=\alpha_r=0$; $b_x=b_r=b_h=b_\theta=0.5$. The viscoplastic parameters c_{xd}, c_{rd}, c_{hd}, and $c_{\theta d}$ are deliberately set equal to 0.4 (for reasons explained in the second companion paper [1]). The other parameters are not relevant for fully bonded conditions at the caisson–soil interface. The strength parameters: maximum soil resistance permit depth, p_y, maximum resisting moment per unit depth, m_y, and shear Q_{by} and moment capacity M_{by} at the base of the caisson, were back-calculated from preliminary finite element analysis to be consistent with the Von-Mises yield criterion. The following approximate expressions were derived

$$p_y \approx 8S_uB \tag{17}$$

$$m_y \approx S_uB^2 \tag{18}$$

$$Q_{by} \approx \frac{\pi}{4}S_uB^2 \tag{19}$$

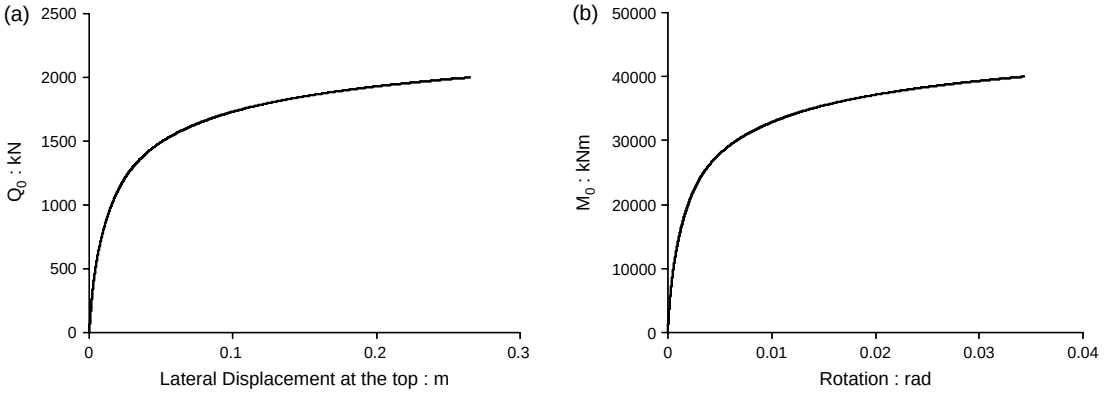

Fig. 15. (a) Horizontal force–displacement and (b) moment–rotation curves at the top of the caisson ('pushover' curves).

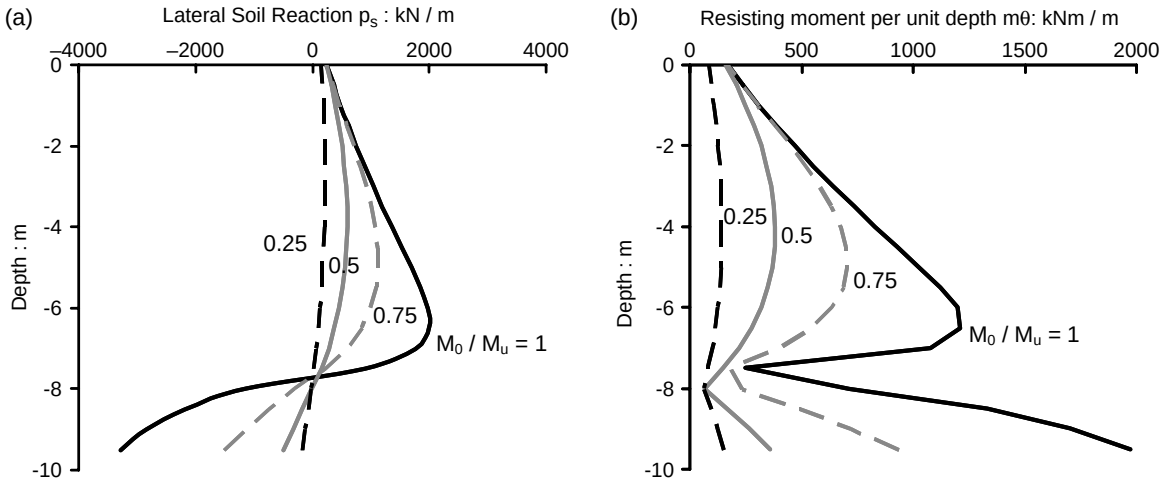

Fig. 16. Distributions with depth of: (a) horizontal soil reaction p_s, and resisting moment m_θ for different stages of loading (in terms of the applied moment to the ultimate moment capacity of the caisson, M_0/M_u). Static loading test.

and

$$M_{by} \approx \frac{2}{5}\pi S_u B^3 \tag{20}$$

Notice, that the theoretical value of p_y ranges between $6S_uB$ and $12S_uB$; the lowest value being approximately the plasticity solution for the bearing capacity of a surface footing [6] and the highest value of a deeply embedded footing with rough footing-soil interface [7]. Eq. (20) gives values for M_{by} which are twice as large as for surface footings [8], reflecting the beneficial effect of embedment.

Fig. 3 compares the finite element and the developed Winkler model results for (a) the horizontal force–displacement and (b) the horizontal force–rotation curves at the top of the caisson ('pushover' curves) for Case A1. The comparison is generally satisfactory. Fig. 4 shows the evolution of soil yielding computed from the finite element analysis. Note, that soil plastification initiates in the vicinity of the caisson head at small strain levels and as the load increases extends progressively to greater depths ($t=0.82$ and 0.93) and even below the base of the caisson ($t=1$). Recall by contrast, that in case of a *pile* only a small upper part (its 'active' length) participates in the failure pattern [5]. Contours of lateral displacement at different stages of loading are depicted in Fig. 5. The maximum attained displacement and rotation were found to be about 12 cm and 0.023 rad, which are in broad agreement with those predicted by the proposed model.

Comparison of the force–displacement and moment–rotation curves between the two methods of analysis for subcase A2 (combined shear force of 1.5 MN and overturning moment of 15 MNm monotonically applied), is given in Fig. 6. The comparison is fairly satisfactory. Fig. 7 portrays the evolution of soil yielding with increasing load. Notice that the failure pattern differs from that observed in subcase A1. In this case, plastification of the soil initiates almost simultaneously in the vicinity of the head *and* the base of the caisson, and then propagates towards the middle depth of the caisson with increasing strain level. The difference in the two failure patterns reflects the influence of the relatively large applied overturning moment which increases the load transmitted through the base.

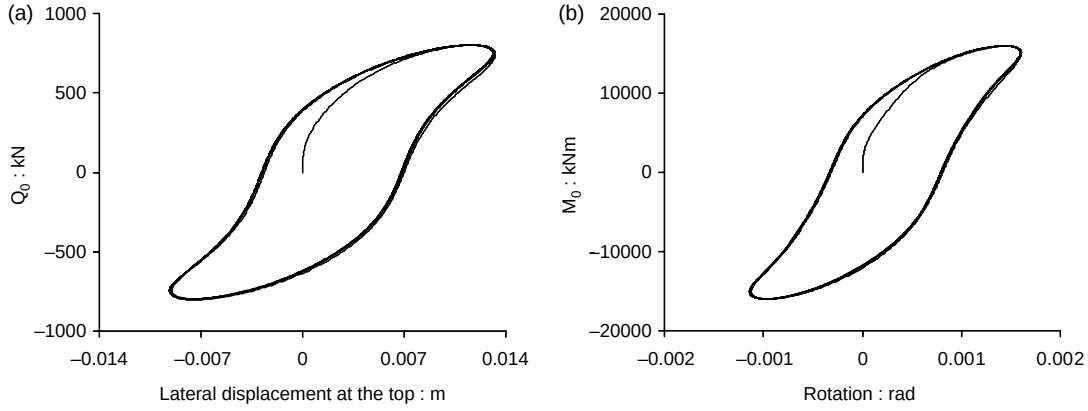

Fig. 17. (a) Horizontal force versus displacement and (b) overturning moment versus rotation loops at the top of the caisson, for Case b1 (only *soil* nonlinearity is considered).

In the second case, the caisson is subjected to dynamic loading. The fundamental period of the caisson–soil system, about 1.5 Hz, is smaller than the frequency of loading; hence full radiation damping is expected to develop. The global force–displacement and force–rotation loops atop of the caisson for the finite element and the proposed method are compared in Fig. 8, for the first subcase. The sharpness of the loops predicted by the Winkler model is characteristic of the extensive soil plastification at large displacements which cause a decrease in radiation damping. However, in unloading, where the caisson–soil system behaves almost elastically the contribution of radiation damping to the overall response increases resulting in a widening of the loop. The finite element method computes smoother loops implying an underestimation of the coupling between hysteretic and radiation damping. Notice also, that both models predict asymmetric loops with respect to loading direction. This reflects the severe soil yielding developed during the first loading half-cycle which results in a permanent shift of the caisson base. The maximum attained displacement and rotation in the finite-element analyses were found to be approximately 11 cm and 0.021 rad, in the positive direction of loading, and 6 cm and 0.011 rad in the negative direction of loading (the corresponding values of our model are about: 9.5 cm and 0.21 rad in the positive, and 5.8 cm and 0.012 rad in the negative direction).

Fig. 9 plots the force–displacement and moment–rotation loops at the top of the caisson calculated by the finite element and the Winkler model, for the second subcase (B2). The agreement between the two methods of analysis is indeed quite satisfactory.

It is pointed out that all the above comparisons were performed using the same values of the parameters of the

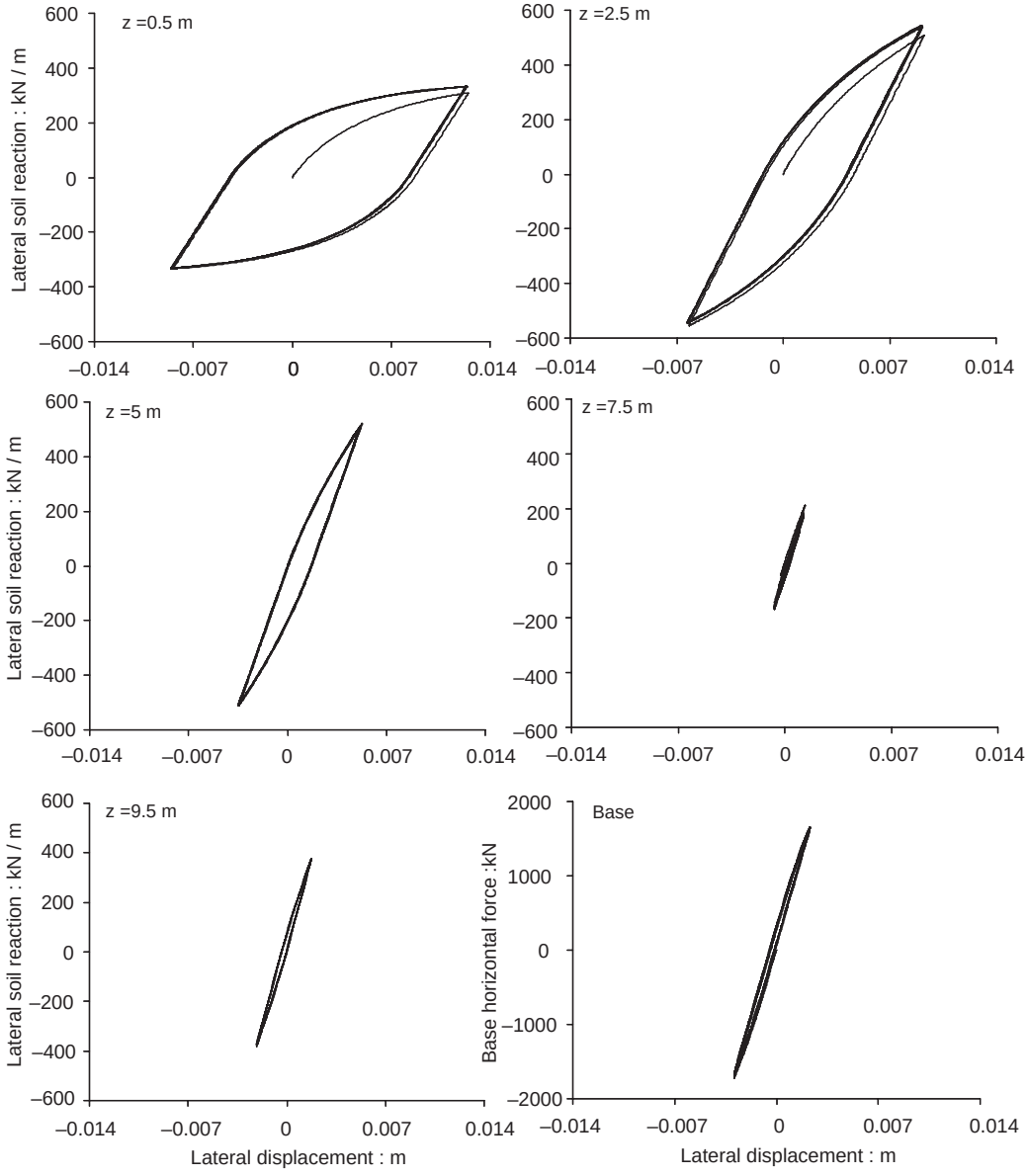

Fig. 18. Horizontal soil reaction versus displacement loops at five selected depths and at the base of the caisson, for Case b1 (only *soil* nonlinearity is considered).

proposed model. In other words, re-calibration of the model parameters was not performed in each analysis, revealing the capability of the proposed model to reproduce the response of the caisson under different loading paths.

4. Tentative validation of the method: scaled field experiments on statically loaded caisson

The method developed in the companion paper and outlined in the Section 3 herein emphasized the nonlinear inelastic phenomena associated with large deformations and near-failure conditions of a laterally loaded caisson. Verification of the method, an absolutely necessary pre-requisite for adopting it in practice, is not a trivial task. Small scale tests (e.g. on a shaking table) are not appropriate, since the unavoidable scaling effects are likely to severely distort not only soil failure conditions, but also phenomena such as separation and sliding at interfaces, which are precisely what our methods aspires to simulate. That is why the 1/3-scale load tests in the field, conducted on behalf of the Electric Power Research Institute (EPRI), California, are of particular significance and are utilized herein [3]. Soil parameters were established from laboratory and in situ measurements. The test studied here employed a cylindrical caisson of diameter $B=1.524$ m and height $D=4.115$ m (slenderness ratio $D/B=2.7$). The caisson was embedded in a moderately stiff–stiff clay, underlain by a soft schist on top of which the caisson was founded. Soil properties and caisson characteristics as given in the original publication are shown in Fig. 10. The caisson was subjected to a pure moment loading at its head, 0.305 m above groundline, until 'failure'.

The parameters of the model were calibrated from back-analysis of the measured caisson response. The following

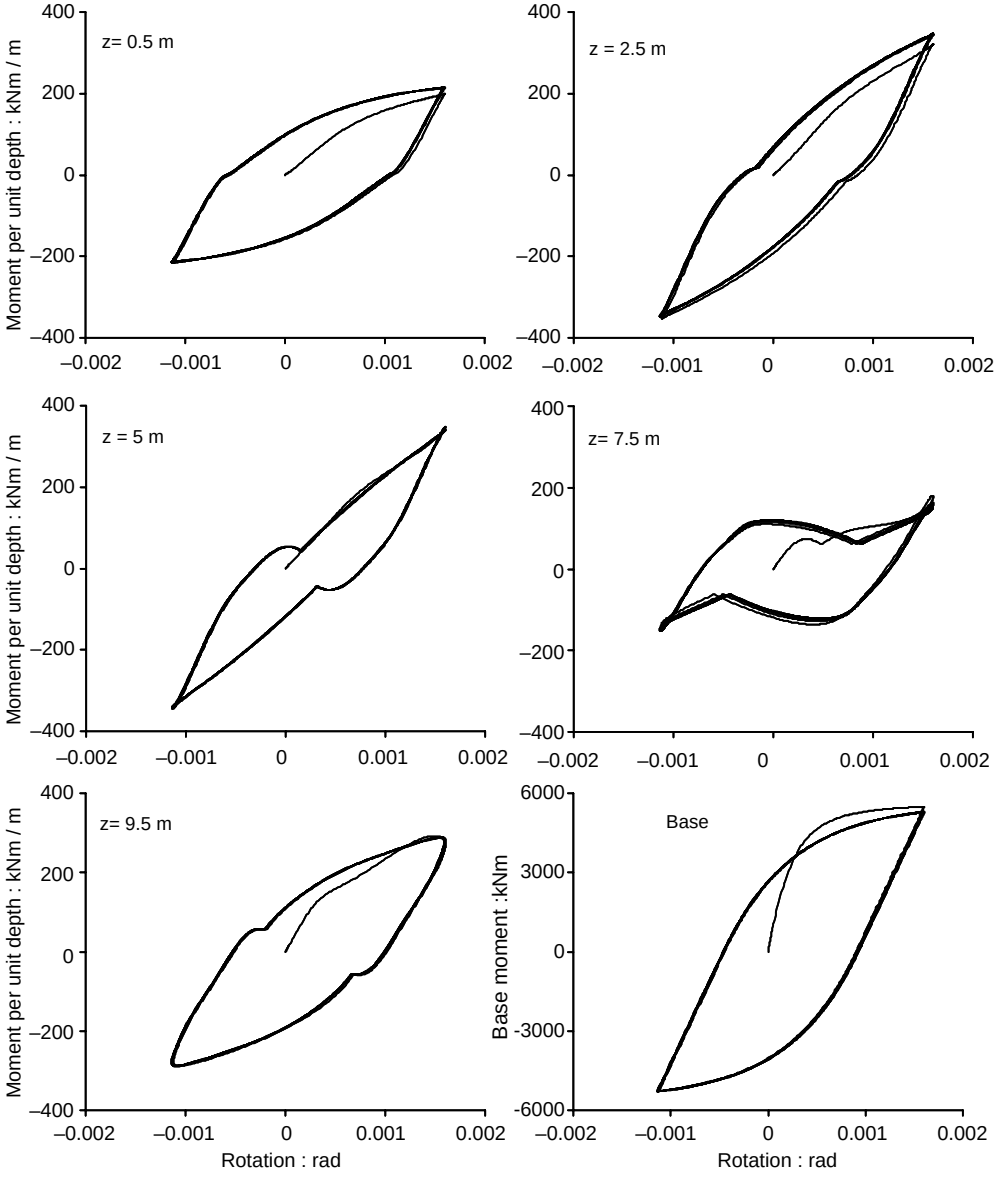

Fig. 19. Resisting moment per unit depth versus rotation loops at five selected depths and at the base of the caisson, for Case b1 (only *soil* nonlinearity is considered).

values were obtained: For the moderately stiff clay: $n_x=0.6$, $\alpha_x=0$, $b_x=0.5$, $n_\theta=2$, $b_\theta=0.5$. For the stiff clay: $n_x=0.05$, $\alpha_x=0$, $b_x=0.5$, $n_\theta=2$, $b_\theta=0.5$. For the soft schist (at the base of the caisson): $n_h=2$, $b_h=0.5$, $n_r=3$, $\alpha_r=0$, $b_\theta=0.9$. The interface parameters were assumed to be: $\phi_b=30^\circ$ and $\delta_{int}=30^\circ$. For details on the role of each parameter in the response of the caisson, the reader is referred to the second companion paper [1].

Surprisingly, the parameter n_x, for monotonic loading of the lateral soil reaction was found to be much larger for the moderately stiff clay than the one for the stiff clay, whereas one might have expected the opposite. Several alternative hypotheses have been advanced to explain this paradoxical behaviour. For instance: (a) only the upper part of the caisson (embedded in the [moderately stiff clay]) deflects, while the lower part remains practically inactive (due to the small caisson–soil stiffness contrast, E_p/E_s, in the stiff clay layer). This means that the caisson behaves as a flexible and not as a rigid body as modeled in the present study. This is reminiscent of the 'active' length of a pile subjected to lateral loading [5,9]. (b) The caisson is not in good-contact with the stiff clay layer.

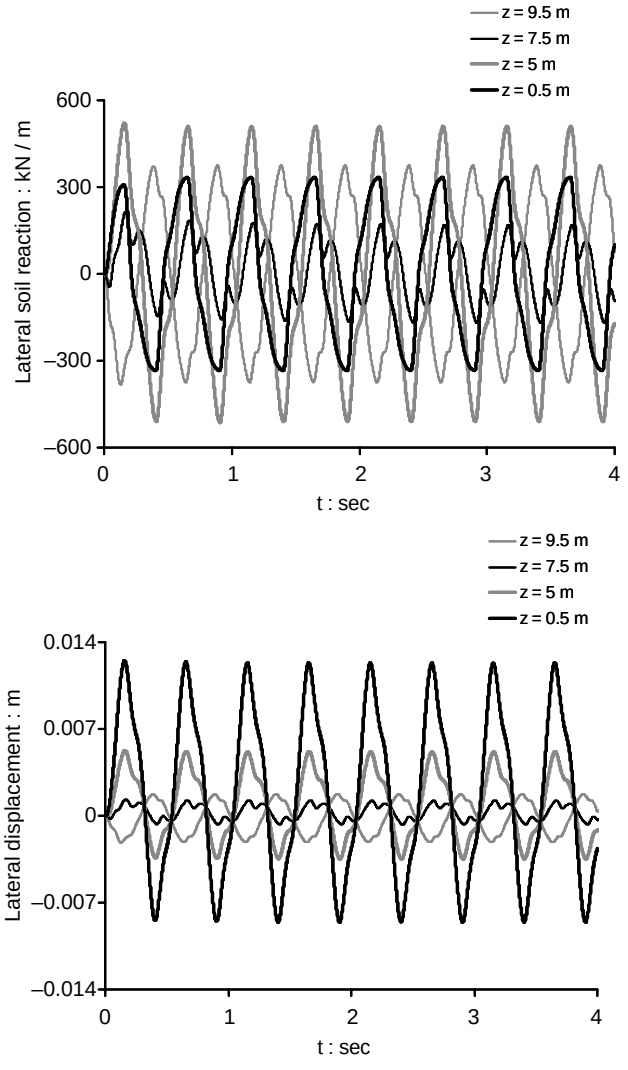

Fig. 20. Time histories of lateral soil reaction (top) and the related displacement (bottom) at four selected depths, for Case b1 (only *soil* nonlinearity is considered).

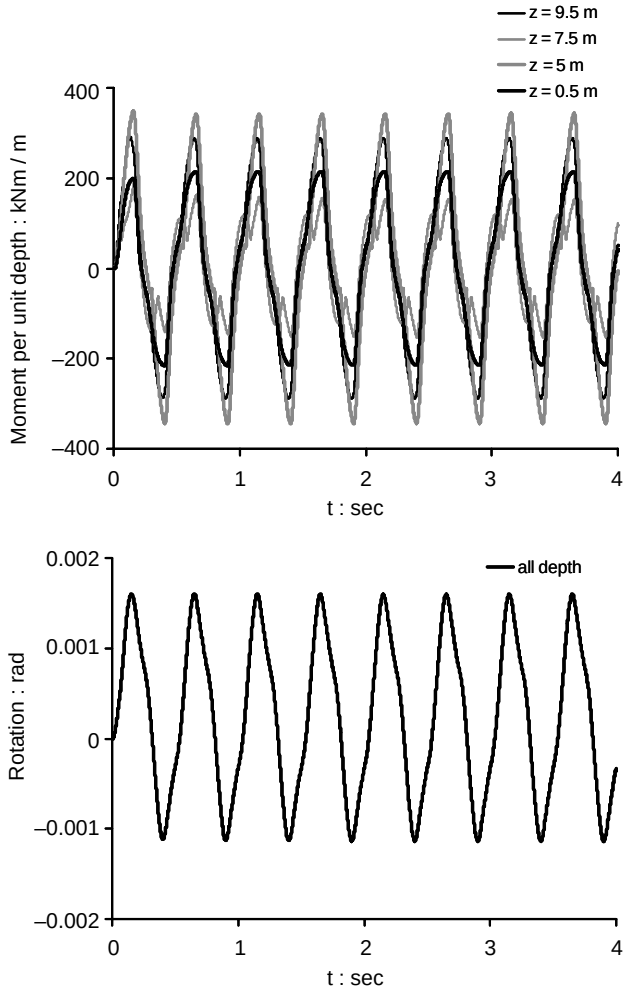

Fig. 21. Time histories of resisting moment per unit depth (top) and related rotation (bottom) at four selected depths, for Case b1 (only *soil* nonlinearity is considered).

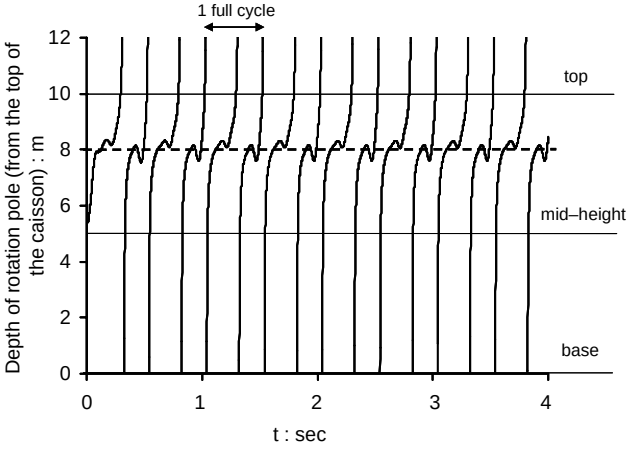

Fig. 22. Evolution of the location of the rotation pole of the caisson (solid line), for Case b1 (only *soil* nonlinearity is considered). The dotted line corresponds to the per cycle average depth of the rotation pole.

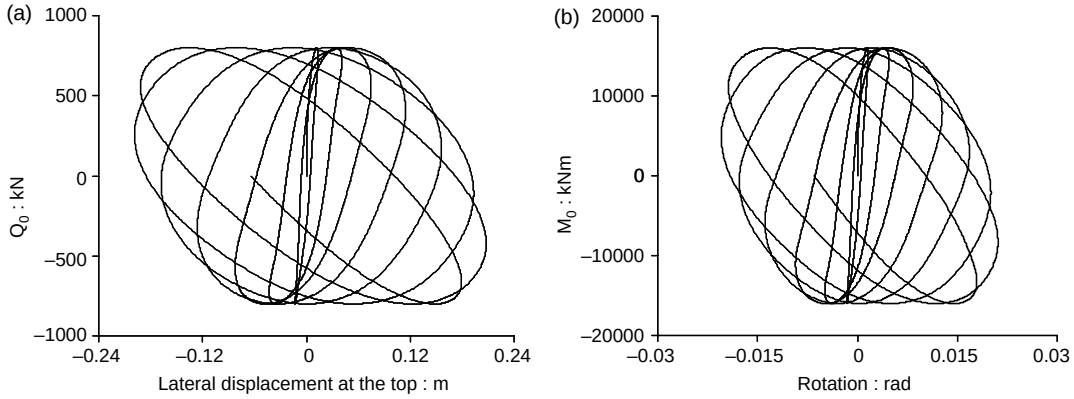

Fig. 23. (a) Horizontal force versus displacement and (b) moment versus rotation loops at the top of the caisson, for Case b2 (both *soil* and *geometrical* nonlinearities are considered).

Since, the measured results [3] indicated that the caisson behaved indeed as a rigid body, only the second assumption could be possibly true.

Fig. 11 plots the distribution of lateral soil reaction when the applied moment, M_0, is equal to one-half of the ultimate moment, M_u. The comparison between the computed with NL-CAISSON solid curve and the experimental data points is reasonably good, especially for the uppermost third of the caisson. The small differences observed at greater depth could be possibly attributed to inaccuracies in the soil parameters as used in our analysis, based on the recommendation of the ERRI report.

However, in spite of this disparity between theoretical and experimental lateral soil reaction, the overall moment–rotation and moment–displacement curves computed with NL-CAISSON are in excellent agreement with the experimental points in Fig. 12. *The 'forgiving power' of integration* must have played a role: local small deviations from reality of one response quantity are balanced by similar but opposite-sign deviations of another quantity, and their effects are masked in the resulting global force–displacement response.

The distribution with depth of the lateral soil reactions, p_s, and resisting moments, m_θ, computed for different stages of loading are plotted in Fig. 13. The variable parameter in these plots (indicating the stages of loading) is the ratio of the applied moment to the ultimate moment ($\approx$4000 kNm). One of the interesting conclusions is that the plastification of clay around the pile begins near the top at an early stage of loading ($M_0/M_u = 0.50$). At higher M_0/M_u values the plastified zone extends deeper; for $M_0/M_u = 0.75$ almost one-half of the caisson experiences the maximum possible resistance (p_{ult}, $m_{\theta,ult}$). Observe in this zone a softened caisson response despite the appreciable initial stiffness of the soil. On the other hand, below the point of rotation (located at about 1.6 m from the base) the ultimate (passive) resistance is being reached only when M_0/M_u is close to unity.

5. Parametric study of caisson–soil interaction to lateral static and cyclic loading

The developed model is further utilised to study the problem sketched in Fig. 14: a reinforced concrete caisson of $D = 10$ m height and $B = 5$ m diameter, embedded in cohesive soil, undergoes lateral loading. Young's modulus and undrained shear strength of the soil increase linearly with depth. The caisson supports a 20 m high bridge pier and its deck. As a result of the seismic inertial response of the bridge the caisson is subjected to a combined shear force Q_0 and bending moment $M_0 = 20\ Q_0$. The vertical force transmitted down to the base of the caisson is assumed to be equal to 5 MN, which is about the 1/3 of the ultimate vertical load capacity of the caisson base. At such a relatively high safety factor against bearing capacity failure, uplift is the most likely dominant 'failure' mechanism of the base during dynamic loading (Apostolou and Gazetas [4]).

Two cases are considered:

(a) the load is applied monotonically until complete 'failure' of the caisson–soil system, and
(b) eight cycles of a 2 Hz sinusoidal time history of horizontal force of amplitude $Q_0 = 0.8$ MN, and overturning moment of amplitude $M_0 = 16$ MNm is applied. For this second case, two subcases are studied:
  (b1) only soil inelasticity is considered, and

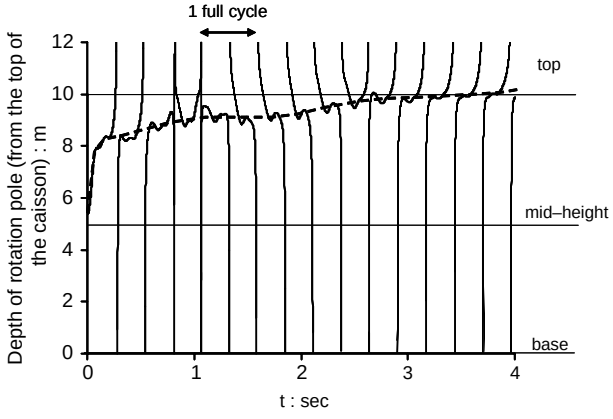

Fig. 24. Evolution of the location of the rotation pole of the caisson, for Case b2 (both *soil* and *geometrical* nonlinearities are considered). The dotted line corresponds to the per cycle average depth of the rotation pole.

(b2) both geometrical nonlinearity and soil inelasticity are considered.

In all cases, radiation damping generated by the caisson is deliberately limited to a 10% of its maximum half space value, to account for the fact that the effective period of the superstructure-foundation system, likely to be of the order of 1 s for a typical bridge, would be larger than the first natural period of the soil. The yielding criterion for the caisson–soil interface is assumed to be pressure dependent. This means that the maximum resisting moment per unit depth of the caisson increases with increasing lateral soil reaction.

The values of the parameters used in the analyses are: $n_x=1$, $n_\theta=3$, $n_h=3$, $n_r=1$, $\alpha_x=0$, $\alpha_r=0$, $b_x=0.5$, $b_\theta=0.5$, $b_h=0.5$, $b_r=0.5$ (0.9 for subcase b2), $\phi_b=30°$, $\delta_{int}=30°$, and $c_{xd}=c_{\theta d}=c_{rd}=c_{hd}=0.3$. For subcase b2, only the pinching parameters δ and ζ_0 were set equal to 0.054 and 0.99, respectively.

The monotonic force–displacement and moment–rotation curves at the top of the caisson are presented in Fig. 15 and reveal a highly nonlinear response. Failure is practically achieved when the applied horizontal force and overturning moment at the top reach the values of about 2 MN and 40 MNm, respectively, corresponding to a displacement of 26 cm and a rotation of 0.035 rad.

The detailed distributions with depth of the computed horizontal soil reaction, p_s, and resisting moment, m_θ, (resultants per unit depth) at different stages of loading, are depicted in Fig. 16. The parameter is the ratio M_0/M_u, i.e. applied moment to ultimate moment capacity, varying from 25% (almost linear case) to 100% (ultimate load). We notice that the ultimate soil reaction at its top 1 m is being (fully) mobilized already from the time the applied moment is 50% of ultimate moment. Soil yielding extends progressively to greater depths as the load increases. For 75% of ultimate load, soil plastification (i.e. reaching of ultimate soil resistance) extends to 2.5 m below the ground surface.

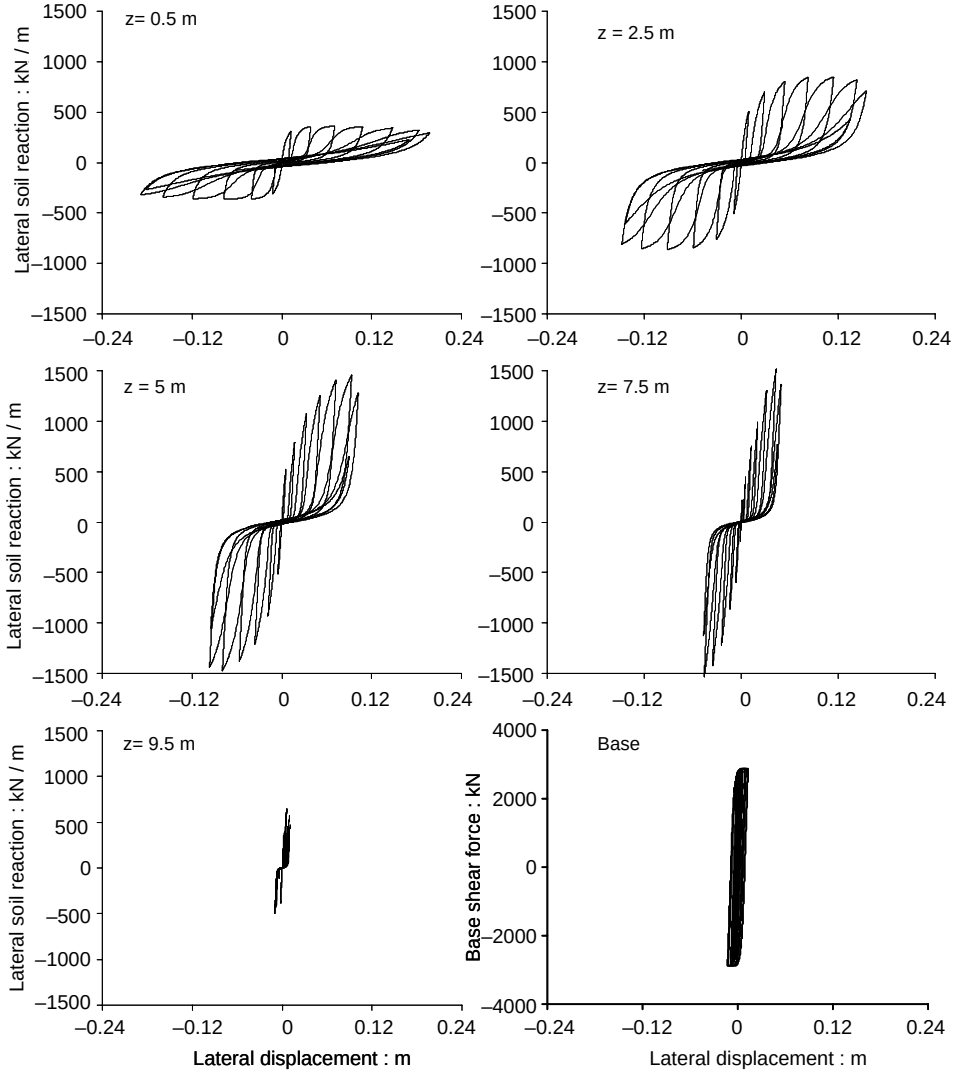

Fig. 25. Lateral soil reaction versus displacement loops at five selected depths and at the base of the caisson, for Case b2 (both *soil* and *geometrical* nonlinearities are considered).

Below the rotation pole (at about 8 m below the ground surface), ultimate (passive) soil reaction is not reached even at 'failure'. It is also interesting to note that in the vicinity of the rotation pole the resisting moment approaches but is never exactly zero despite the fact that the related lateral soil reaction is exactly equal to zero. This is thanks to the earth pressures at rest ($K_0\sigma'_v$)) which contribute to the shear tractions produce the resisting moment at this depth.

In the second case, the caisson is subjected to dynamic loading of amplitude equal to the 40% of its static ultimate capacity (i.e. $M_0=16$ MNm, $Q_0=0.8$ MN). The global force–displacement and moment–rotation loops at the top of the caisson are portrayed in Fig. 17 for the first subcase (i.e. when only soil inelasticity is allowed to occur). The maximum attained displacement and rotation were found to be merely 1.3 cm and 0.0016 rad, respectively.

Figs. 18 and 19 show at five different depths along the shaft of the caisson the hysteresis loops of:

- the local soil reaction, p_s, versus local horizontal displacement, u; and
- the local resisting moment, m_θ, versus the angle of rotation, θ, of the (rigid) caisson,
- the sixth plot in each of these figures is the hysteresis loop of the (resultant) base shear force, Q_{bs}, versus displacement, u_b, and the (resultant) base moment, M_{bs}, versus rotation, θ.

The substantial influence of the confining pressure is very clear on the p_s versus u diagrams: with increasing depth the response of the horizontal spring becomes stiffer and more elastic. Notice of course that this stems from the fact that the lateral displacements at large depths are negligibly small. By contrast, due to the relatively large applied moment on the

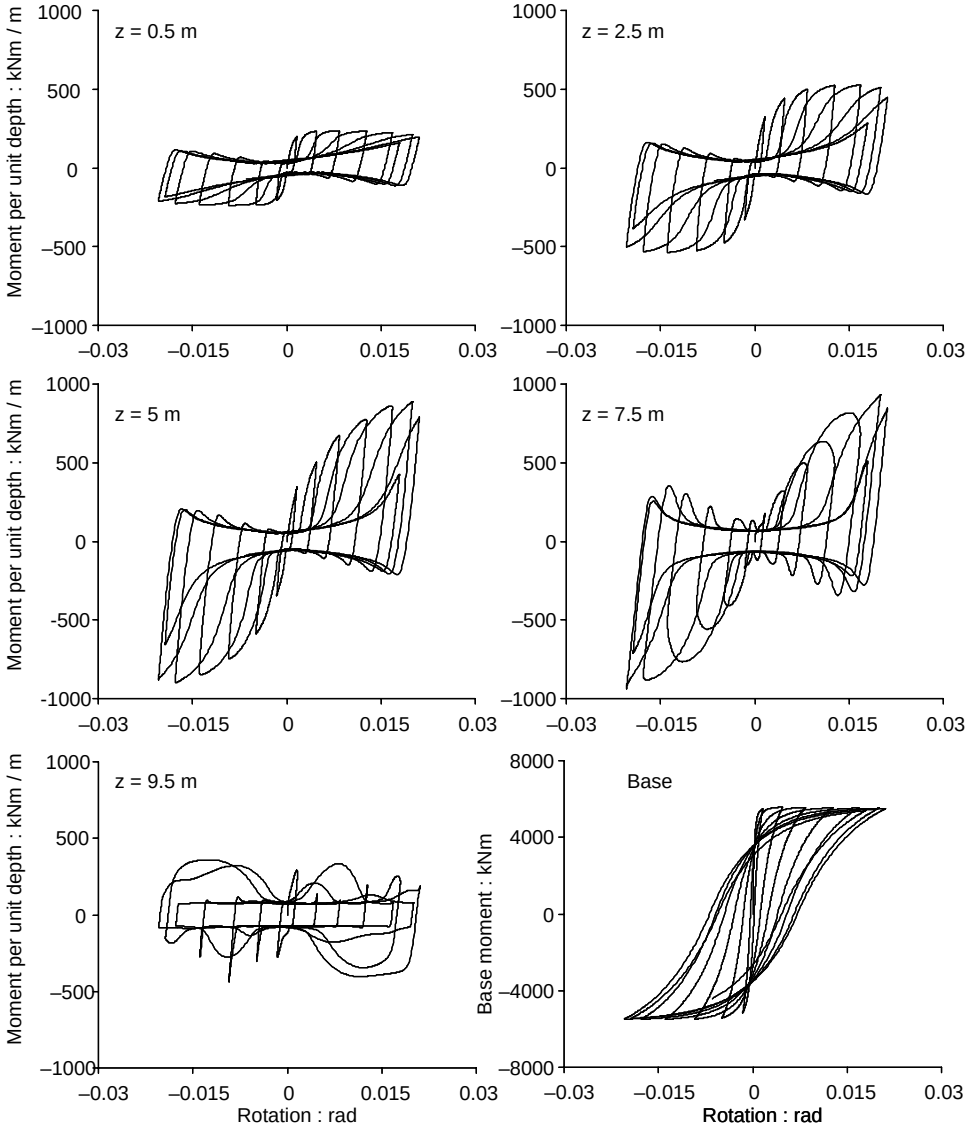

Fig. 26. Resisting moment per unit depth versus rotation loops at five selected depths and at the base of the caisson, for Case b2 (both *soil* and *geometrical* nonlinearities are considered).

caisson, the angle of rotation is also relatively large and, of course, constant with depth. Hence, the m_θ, versus θ loops exhibit significant inelasticity, even at large depths.

The above conclusions are further reinforced by examining Figs. 20 and 21, which portray the time histories, $p_s(t)$, $u(t)$, $m_\theta(t)$, and $\theta(t)$, at four depths (ranging from near $z=0.5$ m the surface to $z=9.5$ m near the base). Notice the in(phase $m_\theta(t)$ response of all points, in contrast with the out-of-phase $p_s(t)$ response above and below the pivot point.

Fig. 22 plots the evolution with time of the location of the rotation pole of the caisson. Notice, that during the first cycle the rotation pole moves rapidly from the caisson center (5 m depth) to a depth of about 8 m, and its location remains nearly unchanged in subsequent cycles. The spikes observed in the time history at the end of each cycle correspond to zero rotation angle and thus to infinite depth of the rotation pole.

Refer now to the second subcase, b2, where both soil and interface nonlinearities are included in the analysis (Figs. 23–28). The global force–displacement and moment–rotation loops at the top of the caisson are presented in Fig. 23. The maximum attained displacement and rotation were calculated to be about 21 cm and 0.02 rad, respectively, which are substantially larger values than those of the first subcase—a detrimental consequence of geometric nonlinearities (gapping and base uplifting). Three modes of oscillation can be distinguished in this figure. In the first cycle, the response of the caisson is quasi-elastic and the rotation pole is located at about the caisson center. In the subsequent two cycles, soil inelasticity dominates upon interface nonlinearities, and the rotation pole moves towards the base of the caisson. The shape of the moment–rotation loop corresponding to those two loading cycles is similar to that of the first subcase (when only soil nonlinearity was considered). In the subsequent loading cycles, however, the gap forming around the caisson is continuously growing up and its influence on the response of the caisson becomes prevalent. The hysteresis loops associated with those cycles continuously change orientation and reach an opposite loading direction (this means positive values of M_0 are related to negative values of

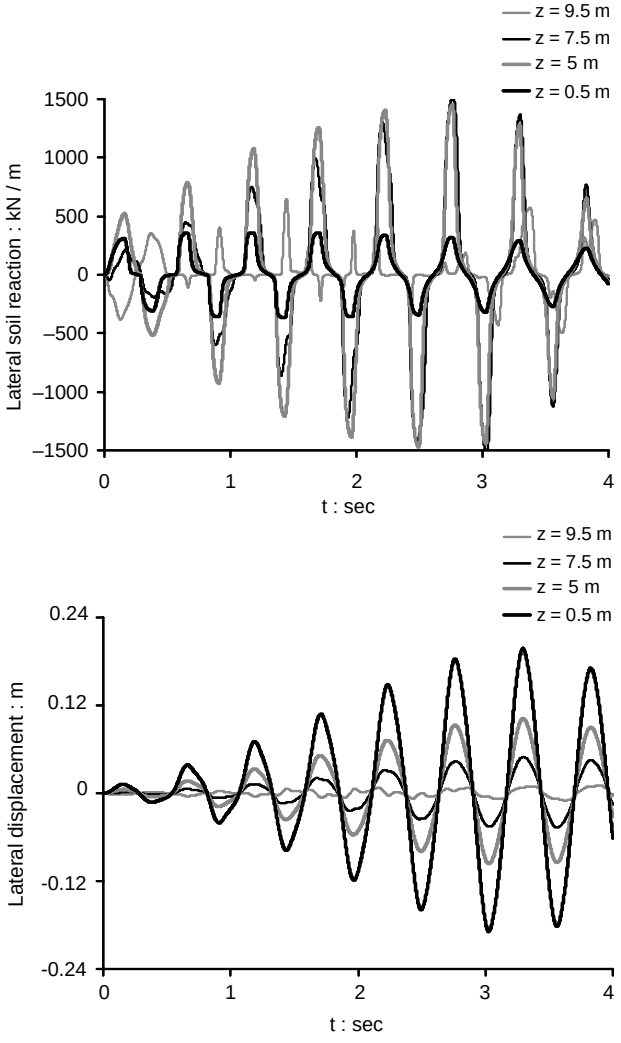

Fig. 27. Time histories of lateral soil reaction (top) and related displacement (bottom) at four selected depths, for Case b2 (both *soil* and *geometrical* nonlinearities are considered).

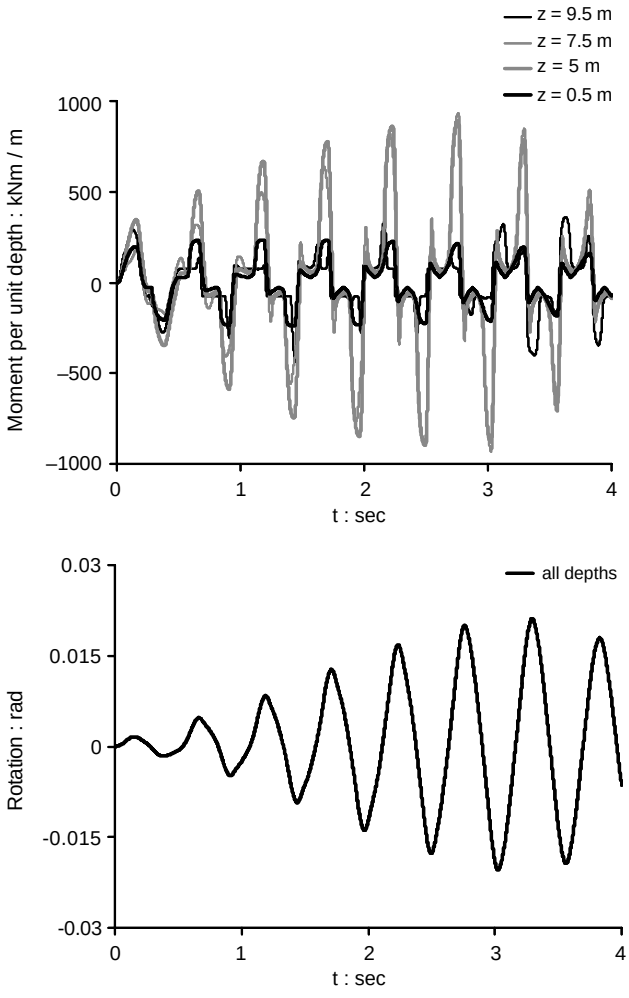

Fig. 28. Time histories of resisting moment per unit depth (top) and related rotation (bottom) at four selected depths, for Case b2 (both *soil* and *geometrical* nonlinearities are considered).

Table 1
Results of dynamic analyses of a caisson ($D=10$ m, $B=5$ m) embedded in clay and subjected to a combined lateral loading ($M_0=20\,V_0$) of sinusoidal time history of eight cycles at 2 Hz, applied at its top

Linear analysis		Nonlinear Analysis (*only soil inelasticity*)		Nonlinear Analysis (*both soil and geometrical nonlinearities*)	
Maximum rotation θ_{max} (rad)	Maximum lateral displacement u_{max} (cm)	Maximum rotation θ_{max} (rad)	Maximum lateral displacement u_{max} (cm)	Maximum rotation θ_{max} (rad)	Maximum lateral displacement u_{max} (cm)
10% of the full radiation damping					
Case c1		Case b1		Case b2	
6×10^{-4}	0.5	0.0016	1.3	0.02	21
Full radiation damping					
Case c2		Case d1		Case d2	
5×10^{-4}	0.4	0.001	0.8	0.003	3

θ—an out-of-phase motion). The rotation pole has now moved below the base of the caisson. The evolution of the location of rotation pole of the caisson is plotted in Fig. 24. This plot should be compared with the corresponding plot of Fig. 22.

Figs. 25 and 26 plot the time histories of the local force and moment reactions, $p_s(t)$ and $m_\theta(t)$, and the corresponding displacements and rotations, $u(t)$ and $\theta(t)$. These plots should be compared with the corresponding plots of Figs. 20 and 21, respectively. Notice that the displacement and rotation amplitudes of the caisson increase almost continuously with time (up to about 3.5 s), despite the imposed harmonic loading. This is attributed partly to the gap forming around the caisson which broadens with increasing number of loading cycles, thereby reducing soil resistance.

Figs. 25 and 26 demonstrate that the developed method is capable of simulating the separation of the caisson from the soil. The bottle-shaped time histories of the hysteretic part of the lateral soil reaction, p_s, are indicative of the apparent gapping. The progressive widening of the gap with increasing number of loading cycles can be better seen in the hysteresis loops of Figs. 27 and 28.

Notice also that the maximum hysteretic lateral soil pressure, p_s, the caisson experiences ($\approx$1,5 MN/m) is about 2.5 times larger than that calculated in the first subcase ($\approx$600 kN/m). This is because the caisson, oscillating inside the gap, meets resistance from the surrounding soil every time it returns and 'hits' with velocity the free(standing 'wall' of the hole.

The abrupt increase in m_θ near the edges of the loops is attributed to the increased lateral soil pressure at those points—a result of gapping. Notice also that at $z=9.5$ m, i.e. at the vicinity of the rotation pole, the resisting moment is very small exhibiting a rectangular-shaped m_s versus θ loop, presumably because no lateral soil reaction develops there and τ_{rz} are due only to the initial K_o stesses.

The sharpness of the resisting moment–rotation loop, M_b versus θ, at the base of the caisson along with the progressive degradation with cyclic loading of the reversal stiffness, is characteristic of base uplifting accompanied with extensive soil plastification. It is rather promising that the proposed simplified model for caissons can capture such a complex nonlinear behaviour.

To further investigate the influence of geometric nonlinearities on the inertial response of a caisson, the following additional analyses were also carried out:

Case (c) linear elastodynamic analysis of the caisson considering: (c1) with a) 10% cut off the radiation damping, and (c2) with full radiation damping.

Case (d) nonlinear dynamic analysis with full radiation damping: (d1) with only *soil* inelasticity considered, and (d2) with both the soil and geometric nonlinearity considered. The results of all the dynamic analyses (Cases: b1, b2, c1, c2, d1, and d2) are summarized for comparison in Table 1, in terms of maximum rotation and displacement atop the caisson. It is concluded that interface nonlinearities (gapping and base uplifting) play an important role in the inertial response of a caisson and must not be neglected in the analysis, although their influence would drastically diminish when the full radiation damping of a homogeneous halfspace is considered.

6. Conclusions

A nonlinear method based on a generalized Winkler model, for the static, cyclic and inertial response of rigid caisson foundations, developed in detail in the companion paper [1] was compared with experimental results, and was subsequently utilized in an numerical study.

Materialized into the code NL-CAISSON, the method reproduces well the results of: (a) 3D-finite element analysis, and (b) an experiment involving a full-scale caisson push-over test from the literature [3].

The numerical study addressed the lateral monotonic and dynamic (sinusoidal-type) response of a caisson embedded in cohesive soil. Two cases were studied: (a) nonlinear response of the soil only, and (b) nonlinear response of both soil (material nonlinearity) and soil–caisson interface (geometrical nonlinearity). It was found out that interface nonlinearities play an important role in the inertial response of a caisson. This role is

amplified when a cut-off frequency for caisson radiation damping exists, and thus radiation damping is minimal.

References

[1] Gerolymos N, Gazetas G. Development of Winkler model for static and dynamic response of caisson foundations with soil and interface nonlinearities. Soil Dyn Earthq Eng, in press, doi:10.1016/j.soildyn.2005.12.002.

[2] Gerolymos N, Gazetas G. Winkler model for lateral response of rigid caisson foundations in linear soil. Soil Dyn Earthq Eng, in press, doi:10.1016/j.soildyn.2005.12.003.

[3] Davidson HL. Laterally loaded drilled pier research. Research report, Electric Power Research Institute, vol. 2. Pennsylvania: Gai Consultants, Inc.; 1982.

[4] Gazetas G, Apostolou M. Nonlinear soil–structure interaction: foundation uplifting and soil yielding. Third joint US-Japan workshop on soil-structure interaction, Menlo Park (California); 2004.

[5] Gazetas G, Dobry R. Horizontal response of piles in layered soils. J Geotech Eng ASCE 1984;110:20–40.

[6] Terzaghi K. Theoretical soil mechanics. London: Wiley; 1943.

[7] Randolph MF, Houlsby GT. The limiting pressure on a circular pile loaded laterally in cohesive soil. Geotechnique 1984;34(4).

[8] Taiebat H, Carter JP. Numerical studies of the bearing capacity of shallow footings on the cohesive soil subjected to combined loading. Geotechnique 2000;50(4):409–18.

[9] Randolph MF. The response of flexible piles to lateral loading. Geotechnique 1984;31(2):247–59.